Microfluidic-Assisted Blade Coating of Compositional Libraries for Combinatorial Applications: The Case of Organic Photovoltaics

Xabier Rodríguez-Martínez, Semih Sevim, Xiaofeng Xu, Carlos Franco, Paula Pamies-Puig, Laura Córcoles-Guija, Romen Rodriguez-Trujillo, Francisco Javier del Campo, David Rodriguez San Miguel, Andrew J. deMello, Salvador Pané, David B. Amabilino, Olle Inganäs, Josep Puigmartí-Luis,* and Mariano Campoy-Quiles*

Microfluidic technologies are highly adept at generating controllable compositional gradients in fluids, a feature that has accelerated the understanding of the importance of chemical gradients in biological processes. That said, the development of versatile methods to generate controllable compositional gradients in the solid-state has been far more elusive. The ability to produce such gradients would provide access to extensive compositional libraries, thus enabling the high-throughput exploration of the parametric landscape of functional solids and devices in a resource-, time-, and cost-efficient manner. Herein, the synergic integration of microfluidic technologies is reported with blade coating to enable the controlled formation of compositional lateral gradients in solution. Subsequently, the transformation of liquid-based compositional gradients into solid-state thin films using this method is demonstrated. To demonstrate efficacy of the approach, microfluidic-assisted blade coating is used to optimize blending ratios in organic solar cells. Importantly, this novel technology can be easily extended to other solution processable systems that require the formation of solid-state compositional lateral gradients.

1. Introduction

Control of compositional gradients has been exploited in multiple materials to engineer new physical and chemical properties as well as novel functionalities. For example, gradual changes in absorption can be used to create tunable density filters,[1] and subtle variations in surface energy can drive water drops uphill.[2] Additionally, compositionally graded materials allow the investigation of the role of compositional effects on a desired property of interest. Examples in this respect include the screening of biochemical signals on cell behavior,[3] the maximization of piezoelectric coefficients,[4] the rapid exploration of material blend phase diagrams,[5] as well as the determination of the optimum composition in ternary photovoltaic devices.[6]

Material libraries are of increasing interest in printed electronics.[7] Indeed,

X. Rodríguez-Martínez, P. Pamies-Puig, L. Córcoles-Guija,
Dr. R. Rodriguez-Trujillo, Dr. M. Campoy-Quiles
Instituto de Ciencia de Materiales de Barcelona
ICMAB (CSIC)
Esfera UAB
Campus Universidad Autónoma de Barcelona
Bellaterra, Barcelona 08193, Spain
E-mail: mcampoy@icmab.es

S. Sevim, Dr. C. Franco, Dr. D. Rodriguez San Miguel, Prof. A. J. deMello,
Dr. J. Puigmartí-Luis
Institute of Chemical and Bioengineering
ETH Zurich
Vladimir Prelog Weg 1, Zurich 8093, Switzerland
E-mail: josep.puigmarti@chem.ethz.ch

The ORCID identification number(s) for the author(s) of this article
can be found under https://doi.org/10.1002/aenm.202001308.

Dr. X. Xu, Prof. O. Inganäs
Biomolecular and Organic Electronics
Department of Physics
Chemistry and Biology (IFM)
Linköping University
Linköping SE-581 83, Sweden

Dr. X. Xu
Department of Materials Science and Engineering
Ocean University of China
Songling Road 238, Qingdao 266100, China

Dr. R. Rodriguez-Trujillo
Department of Electronics and Biomedical Engineering
University of Barcelona
C/Martí i Franquès 1, Barcelona 08028, Spain

Dr. F. J. del Campo
Instituto de Microelectrónica de Barcelona
IMB-CNM (CSIC)
Esfera UAB
Campus Universidad Autónoma de Barcelona
Bellaterra, Barcelona 08193, Spain

feedback between theoretical screening studies[8–11] and high-throughput experimentation[12–14] has accelerated the discovery of new high-performing organic conjugated materials. In the case of organic photovoltaics (OPV), nonfullerene acceptors have recently emerged as promising substitutes for traditional fullerenes as *n*-type semiconductors.[15] On the other hand, polymer:polymer solar cells, which provide a range of printing and stability advantages,[16] start rivaling polymer:fullerene power conversion efficiencies.[17–20]

In a fundamental sense, each novel material combination requires an independent evaluation with regard to photovoltaic performance. The optimization of bulk heterojunction organic solar cells entails the exploration of a highly complex parameter landscape of mutually interacting variables, including the choice of solvent, solution concentration, casting temperature, donor to acceptor (D:A) ratio, film thickness, and annealing temperature.[21] The exploration of such a complex parametric space usually involves a classical sample-by-sample methodology (an Edisonian approach), which is often prohibitively costly in terms of both experimental time and resources. Indeed, discrete sampling remains the primary optimization protocol followed by most researchers in the OPV field, a fact that significantly limits the rate of materials screening and throttles the development of novel high performing devices. Accordingly, the use of combinatorial approaches based on gradients in the parameters of interest (such as film thickness,[12,22,23] morphology,[12,23] and composition[5,6,12,24–26]) represents an ideal route to accelerating such screening processes.[27,28] Whilst several approaches, based on the combination of design-of-experiments and machine-learning algorithms[29,30] as well as robotized laboratories,[31,32] have been used to address the challenges of high-throughput multiparametric screening, these methods generally require either large amounts of raw materials to fully explore the parametric space (rendering them suitable only when optimized synthetic routes or large synthetic batches are readily available)[24] or have limited reproducibility and are restricted to precise processing conditions in terms of ink rheology.[12] In this regard, more versatile experimental procedures are still needed in order to explore the entire parameters versus performance landscape in such complex optimization scenarios in a cost- and material-efficient manner.

Microfluidic technologies can be highly useful in generating compositional libraries in solution. Early reports in this regard date back to 2000,[33] with more recent studies highlighting

Dr. F. J. del Campo
BCMaterials
Basque Center for Materials
Applications and Nanostructures
UPV/EHU Science Park, Leioa 48940, Spain
Dr. F. J. del Campo
IKERBASQUE
Basque Foundation for Science
Bilbao 48011, Spain
Prof. S. Pané
Institute of Robotics and Intelligent Systems
ETH Zurich
Tannenstrasse 3, Zurich 8092, Switzerland
Prof. D. B. Amabilino
School of Chemistry
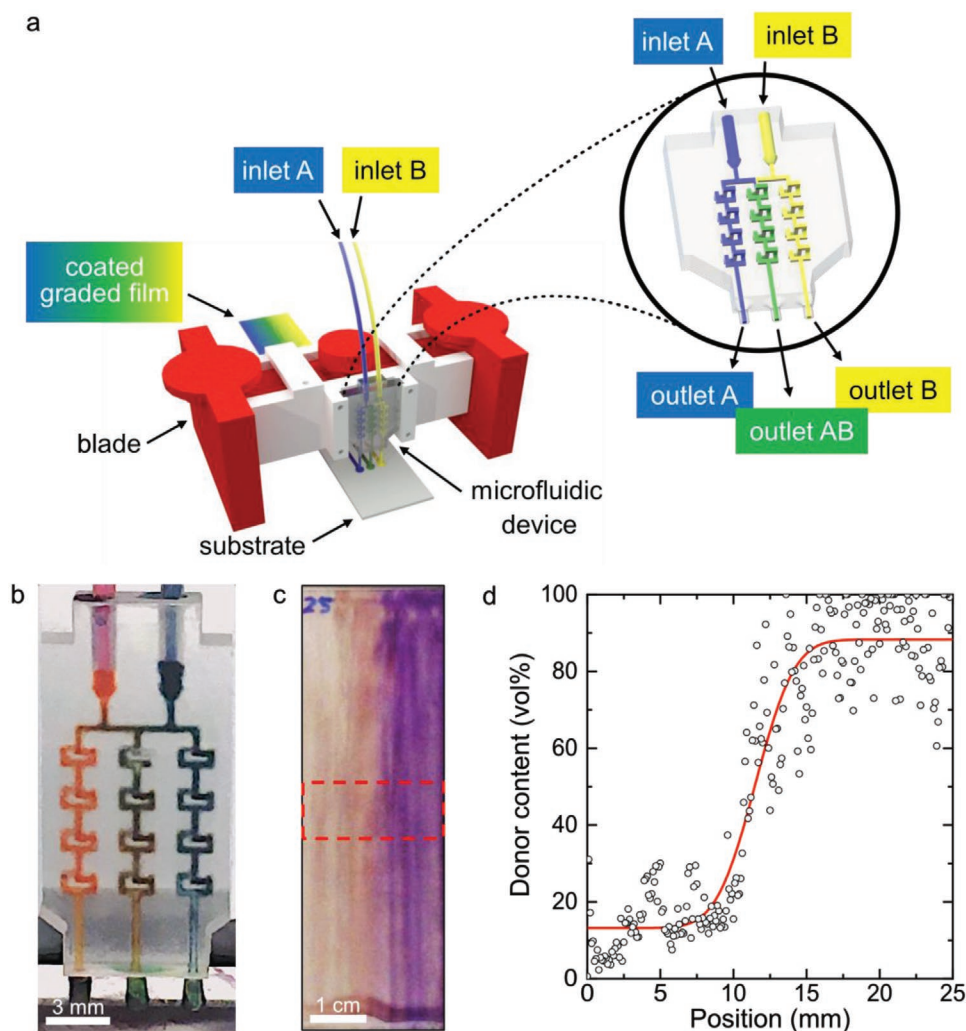University of Nottingham
Nottingham NG7 2RD, UK

utility in fields ranging from biology[34] to electronics.[35] In most of these investigations the generated compositional profiles are exploited directly in the liquid-state, with their transfer to solid films being far from straightforward. Microfluidic-based drop casting experiments have been used to optimize organic thin film transistors,[36] as well as transparent conductive electrodes.[37] However, these approaches are unsuitable for most applications in which large areas of nanometer-thick material films are required. Accordingly, advanced mixing and casting methodologies are urgently required to address all such demands.

Herein, we introduce a completely new microfluidic approach for the generation of solid-state thin films with lateral compositional gradients. Films are formed by blade coating of solutions delivered from the outlet channels of a microfluidic device. We show that such approach enables the efficient and large area transfer of compositional gradients generated in solution to solid state thin films onto virtually any substrate. Additionally, we show that the solid-state lateral composition profile of these microfluidically produced thin films can be finely tuned by the variation of the processing conditions, such as the total flow rate and blade coating speed. To demonstrate efficacy, we specifically optimize the chemical composition as well as the performance of polymer:polymer blend-based organic solar cells. Such systems represent a formidable challenge, due to their intrinsic high viscosities and difficult mixing dynamics.

2. Results and Discussion

To generate a binary compositional gradient, we utilized a microfluidic mixer incorporating two inlets (one for each of the pristine solutions) and a symmetric branched manifold that allows the distribution of the two precursor solutions into three different streams. The three streams are then directly introduced into the blade reservoir to generate a thin film (**Figure 1**a). This symmetric triple-branched microfluidic device can be used to controllably generate solid state binary compositional gradients on surfaces. To ensure the efficient mixing of the two precursor solutions (the blue and yellow solutions in Figure 1a), 3D mixers, such as those based on the baker's transformation,[38] were also considered. Note that these mixing units have been shown to yield the highest mixing efficiencies among passive microfluidic mixers.[39,40] In the current experiments, four interconnected baker's units were used to provide complete and homogeneous mixing at the outlet channels without the need for additional mixing units, such as extended zig-zag microfluidic channels.[41,42] Such a microfluidic design guarantees that only the middle branch generates a mixture of the two pristine precursor solutions that are flowing through the side-branched channels (inset in Figure 1a). Additionally, we systematically explored a variety of outlet configurations, including confluent and individual routing options, as well as slot-die and nozzle-like ejection models (Figures S1–S4, Supporting Information). After a thorough examination of different designs, we concluded that the solid-state compositional profiles obtained when using individual nozzles at the outlet channels were smoother and more reproducible. Moreover, it was observed that the gap between the nozzles and the substrate is key in ensuring continuous fluid ejection during the coating

Figure 1. a) Schematic of the microfluidic-assisted blade coating platform used to fabricate films containing lateral compositional gradients. The inset shows a 3D model of the microfluidic device. b) Image of the microfluidic device under operation with poly(3-hexylthiophene-2,5-diyl) (P3HT, left stream) and poly{[N,N′-bis(2-octyldodecyl)-naphthalene-1,4,5,8-bis(dicarboximide)-2,6-diyl]-alt-5,5′-(2,2′-bithiophene)} (N2200, right stream) dissolved in chlorobenzene. Note that this particular material choice was made to demonstrate generality of the method and to be able to visualize the color contrast in a simple optical image. c) A reflection image of a blade coated film on glass (25×75 mm^2) showing a lateral compositional gradient extending from pure $PC_{70}BM$ (left side) to neat PCDTBT (right side). The observed longitudinal stripes parallel to the coating direction are ascribed to thickness fluctuations. d) Averaged composition profile of the dotted area marked in panel (c) obtained by means of Raman spectroscopy imaging.

process, rather than a dropwise outflow. Dropwise flows eventually result in inhomogeneous films due to Marangoni flows induced in the evaporating drops (**Figure 2**).

We next evaluated the mixing performance and the composition profiles obtained in the films. The marriage of microfluidic solution processing and blade coating aims to transfer the controllable parametric profiles (compositional ratios in the present case) formed in solution (Figure 1b) to a solid-state thin film (Figure 1c). Note that a different blend is shown in each image demonstrating the generality of the method. We focused our initial experiments on polymer:fullerene blends, namely poly[N-9′-heptadecanyl-2,7-carbazole-alt-5,5-(4′,7′-di-2-thienyl-2′,1′,3′-benzothiadiazole)]: [6,6]-phenyl-C_{71}-butyric acid methyl ester (PCDTBT:$PC_{70}BM$), which constitutes a high performing material combination in OPV, and one which has also been recently subjected to combinatorial screening.[12] Accordingly,

we characterized the quality of the mixing and the influence of experimental processing variables (blade velocity and the outflow rate) by directly probing composition in the solid-state. Characterization was performed by Raman imaging (Figure 1d) and modeling according to our previously developed methodology,[12,43] which allows extraction of both composition and photocurrent maps in a single experiment. It should be noted that modeling involved the use of previously reported values of the complex refractive index and Raman cross-section for both materials.[12,43] A simple visual inspection (in reflection mode) of films supported on glass substrates (Figure 1c) immediately suggests the formation of lateral compositional gradients. Additionally, optically dense longitudinal stripes in the coating direction can be seen. According to Raman spectroscopy analysis these stripes can be ascribed to film thickness inhomogeneities that do not perturb the averaged lateral composition profile (Figure 1d).
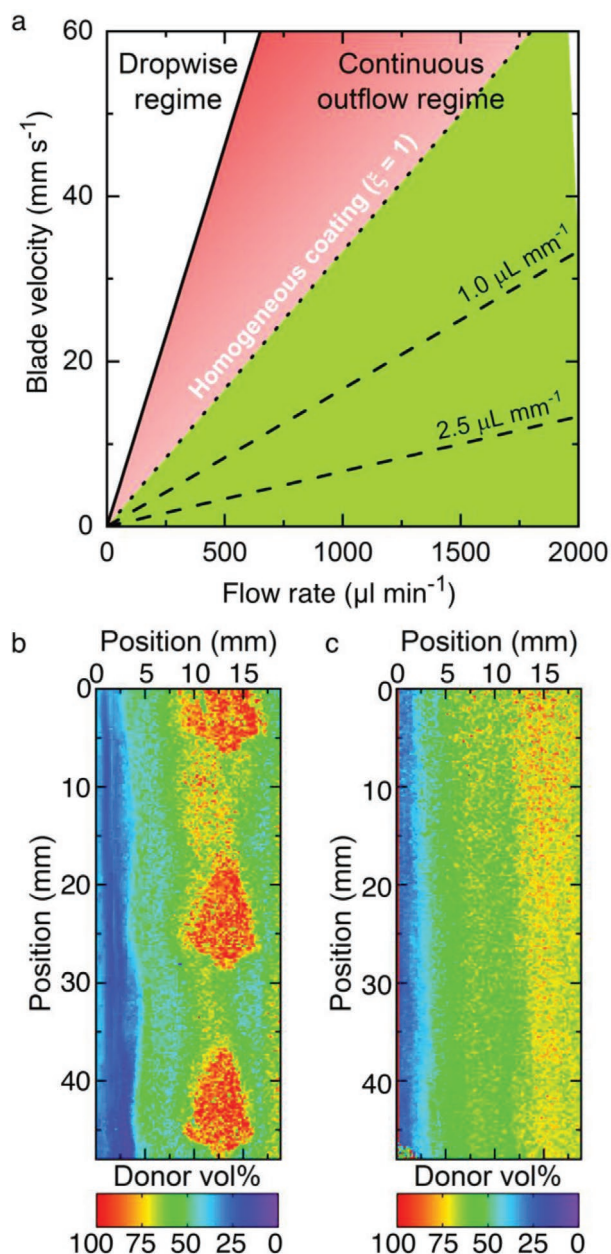
**ADVANCED
SCIENCE NEWS**

www.advancedsciencenews.com

**ADVANCED
ENERGY
MATERIALS**

www.advenergymat.de

Figure 2. a) Outflowing and coating regimes found during the microfluidic-assisted blade coating of films based on a phenomenological and geometrical model. b) Raman spectroscopy mapping for samples made of poly[[2,3-bis(3-octyloxyphenyl)-5,8-quinoxalinediyl]-2,5-thiophenediyl] (TQ1) as donor and N2200 as acceptor reveals that in a dropwise regime, rapid evaporation of liquid drops leads to large inhomogeneities in the solid-state. c) Conversely, when continuous outflow conditions are fulfilled, laterally homogeneous films are realized. These conditions correspond to blade velocities and outflow rates located within the green shaded area in (a). Further details of these regimes and model equations are provided in the Supporting Information.

Experimental investigations indicate that the film processability and the final composition profile are primarily determined by the total flow rate (Φ) and the blade coating speed (v). Φ represents the sum of the flow rates at each inlet, i.e., $\Phi = \Phi_1 + \Phi_2$. We systematically characterized the influence that both Φ and v have on the solid thin film according to the

volumetric linear density (ρ) of solution poured per millimeter of substrate travelled by the blade, i.e., $\rho = \Phi\,v^{-1}$ [μL mm^{-1}]. In this regard, a simple geometrical model that phenomenologically delimits the required balance between Φ and v is provided in the Supporting Information. For simplicity, equal flow rates of precursor solutions (i.e., $\Phi_1 = \Phi_2$) are fixed between 600 and 900 μL min^{-1}, with a total solution volume of 50 μL injected per channel over the course of an experiment. It should be noted that prior to the generation of solid-state compositional gradients a purging step is required to realize stationary flow conditions within the branched-manifold. This step is mandatory when using differing flow rates ($\Phi_1 \neq \Phi_2$) to account for the dissimilar viscosity of the injected solutions (Figure S5, Supporting Information). Blade coating speeds were varied between 5 and 30 mm s^{-1}. It is evident that a tradeoff between Φ and v arises to successfully fabricate solid-state compositional gradients. For example, if Φ is excessively low and v excessively high, processing leads to inhomogeneous material deposition due to an insufficient supply of solution to the blade reservoir (Figure 2).

Figure 3b presents lateral composition profiles obtained for a series of PCDTBT:PC$_{70}$BM films processed at different ρ ratios. These profiles are fitted to the following model equation,

$$f(x) = \frac{a}{2}\,\mathrm{erf}\left(\frac{x-d}{b}\right) + c \tag{1}$$

which generates composition profiles (solid lines in Figure 3b) in analogy with the relationships derived from Fick's diffusion laws (vide infra). Interestingly, it can be observed that the width of the blending area (defined by b in Equation 1) linearly varies with ρ (Figure S6, Supporting Information). This finding indicates that at sufficiently high values of ρ the accumulated solution at the blade reservoir has a longer time to mix and interdiffuse during the coating process than at low ρ values, thus leading to laterally extended compositional profiles. Accordingly, besides the mixing that takes place within the baker's transformation mixers, the interdiffusion of the poured volume accumulated at the ink reservoir will also influence the solid-state compositional profiles.

It should be noted that Equation 1 is qualitatively equivalent to the relationship defined by Fick's second law for diffusion in the case of an initial release of mass at concentration c_0 (corresponding to the central outlet) that diffuses homogeneously over a finite area and with initial boundary conditions of $c_1 = 0$ (left side outlet channel) and $c_2 = 2c_0$ (right side outlet channel). In this case the spatial and temporal evolution of the concentration profile $c(x, t)$ is given by

$$c(x,t) = c_0\left[1 + \mathrm{erf}\left(\frac{x}{\sqrt{4Dt}}\right)\right] \tag{2}$$

where D is the molecular diffusion coefficient. The comparison of Equations 1 and 2 indicates that $b \propto (4Dt)^{1/2}$, a fact that supports the observed broadening of the blending area as a function of the mixing time at the ink reservoir.

Once we had confirmed that the branched microfluidic device was able to produce solid-state compositional gradients with the well-known PCDTBT:PC$_{70}$BM pair, we demonstrated the generality of the approach with two polymers frequently
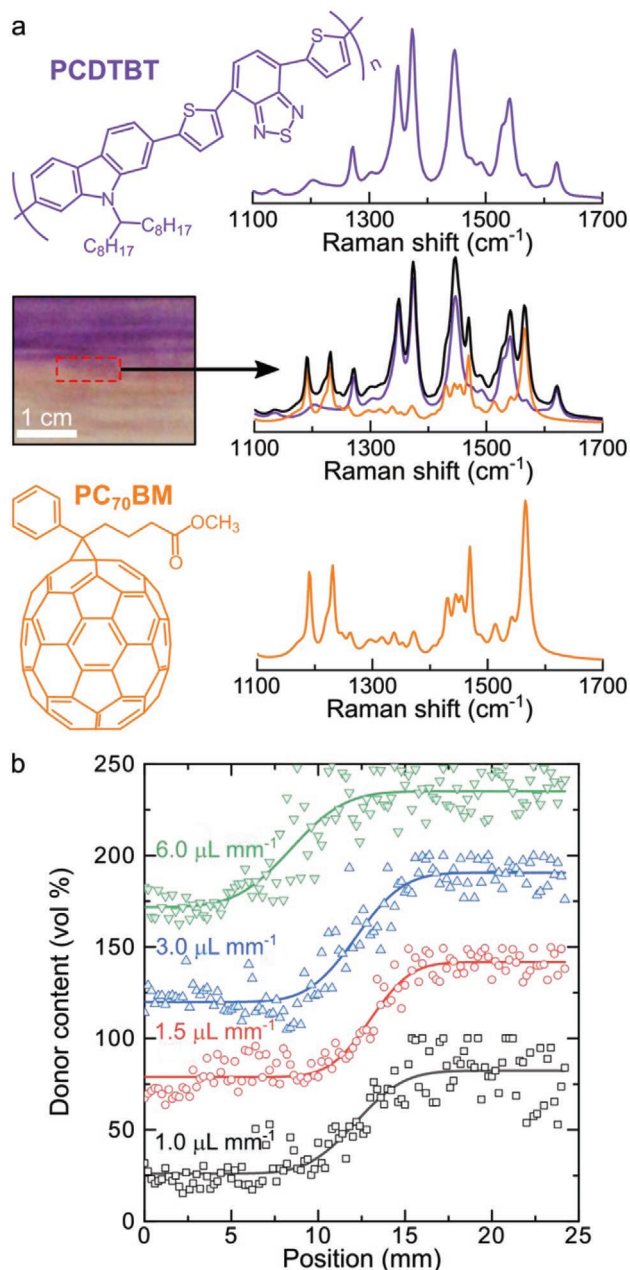
Figure 3. a) Raman spectra measured in PCDTBT:PC$_{70}$BM compositional gradient films can be deconvoluted into the corresponding vibrational fingerprint components for the polymer (purple line) and the fullerene (orange line). Accordingly, the deconvolution serves to quantify the blending ratio.[43] b) Lateral composition profiles for PCDTBT:PC$_{70}$BM films obtained at different volumetric linear densities (ρ). The datasets have been offset along the *y*-axis for clarity.
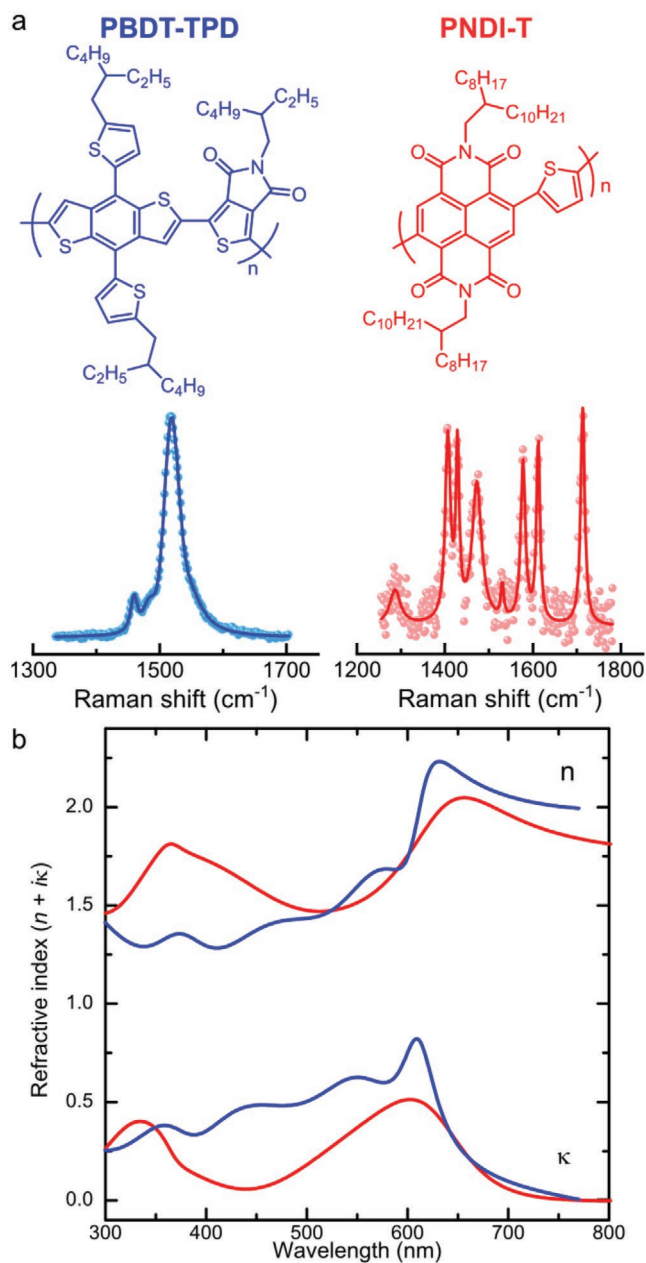

Figure 4. a) Molecular structures and normalized Raman vibrational fingerprints measured using 488 nm excitation of the conjugated polymers PBDT-TPD (blue, donor) and PNDI-T (red, acceptor). b) The corresponding complex refractive indices measured by means of variable-angle spectroscopic ellipsometry (VASE) on blade coated films supported on glass.

used for the fabrication of OPV devices. Specifically, we fabricated large-area organic solar cells comprising a compositional gradient of poly[4,8-bis(5-(2-ethylhexyl)thiophen-2-yl)benzo[1,2-*b*:4,5-*b'*]dithiophene-2,6-diyl-*alt*-(5-(2-ethylhexyl)-4*H*-thieno[3,4-*c*]pyrrole-4,6(5*H*)-dione)-1,3-diyl] (PBDT-TPD) as donor and poly[[*N*,*N'*-bis(2-octyldodecyl)-naphthalene-1,4,5,8-bis(dicarboximide)-2,6-diyl]-*alt*-thiophene-2,5-diyl] (PNDI-T) as

acceptor (**Figure 4**a). The PBDT-TPD:PNDI-T blend constitutes one of the best performing all-polymer combinations currently used for OPV devices.[44] Such solar cells should exhibit a well-controlled lateral compositional gradient in their active layer to enable fast and efficient optimization via concurrent Raman and photocurrent imaging.[12] As for the previous system, elucidation of composition from Raman measurements involved determination of the complex refractive index (Figure 4b) and Raman cross-section (Figures S7 and S8,
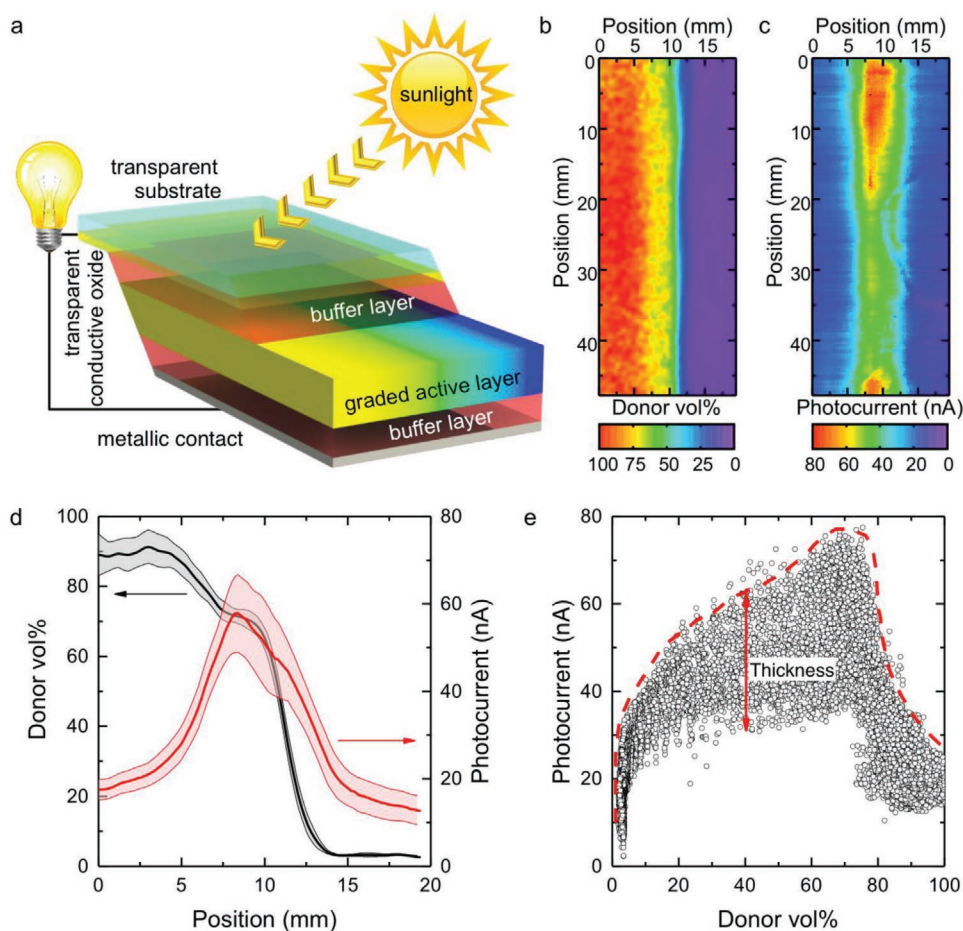
**ADVANCED
SCIENCE NEWS**
www.advancedsciencenews.com

**ADVANCED
ENERGY
MATERIALS**
www.advenergymat.de

Figure 5. a) Schematics and lay-out of an organic solar cell including a compositional gradient in the active layer. The top layers are offset for clarity. b) Composition map of a binary PBDT-TPD:PNDI-T solar cell whose active layer was processed using the microfluidic-assisted blade coating procedure. c) The corresponding photocurrent map of the device measured using 488 nm excitation. d) Averaged lateral composition and photocurrent profiles obtained along the short axis. e) Photocurrent versus donor loading data, including a guide-to-the-eye dashed line that delimits the upper shell of the top performing thickness and blending ratio combinations. The dispersion in the photocurrent axis is ascribed to active layer thickness and morphology variations, as well as to inhomogeneities in the buffer layers.

Supporting Information) for the two polymers. It is important to note that the use of Raman spectroscopy in the determination of composition is particularly useful for materials with overlapping absorption features (as in the current case; Figure 4b) and when high spatial resolution is required.

For processing, the pristine materials were dissolved in chloroform at a concentration of 9 mg mL^{-1}. In the current study, we performed a single ejection (excluding the first transient state prior to steady-state conditions) of 50 µL of solution per inlet to process a device with an area of 25×75 mm^2. This results in a raw material usage below 1 mg per polymer. In addition, the remaining solution can be used for other purposes, and the microfluidic device re-used after cleaning with a suitable solvent.

Figure 5a presents a schematic of the device with an active layer gradient. Figure 5b,c illustrate maps of both composition and photocurrent, respectively, obtained after active layer processing with $\rho = 0.66$ µL mm^{-1}, $\Phi = 1200$ µL min^{-1} and $v = 30$ mm s^{-1}. The compositional map is obtained by quantitatively deconvoluting the corresponding Raman spectra acquired at

488 nm following a previously described methodology[43] and using the refractive index and Raman cross sections obtained from Figure 4 and Figure S8, Supporting Information. The photocurrent map is acquired concurrently using the same 488 nm laser employed as the excitation source for Raman scattering measurements. In this way both the lateral compositional gradient and photovoltaic performance can be efficiently evaluated in a single experiment, generating ≈24 000 data points per device over a period of 2 h.

Figure 5d presents the corresponding averaged composition and photocurrent profiles. It can be seen that the blending ratio varies smoothly between the pure polymer regions, whilst following a profile that resembles those found for the PCDTBT:PC$_{70}$BM films. Conversely, the variation in photocurrent is bell-shaped, suggesting the existence of a relatively narrow optimum blending ratio for the all-polymer photovoltaic blend analyzed here.

These results suggest that beyond polymer:fullerene blends, high-quality and smooth mixing gradients can be blade coated as well in a range of polymer:polymer combinations. In fact, we

**ADVANCED
SCIENCE NEWS**

www.advancedsciencenews.com

**ADVANCED
ENERGY
MATERIALS**

www.advenergymat.de

demonstrate that the microfluidic-assisted processing method works for distinct polymer:polymer mixtures (Figures 1b,2; Figure S9, Supporting Information) and that the compositional profiles obtained are reproducible. However, this is not the case when sticking to the simple coalescence of two drops, which works well for low-viscosity inks[12] but fails in producing controllable gradients when mixing neat polymeric solutions (Figures S10 and S11, Supporting Information).

Removal of the spatial dependence of the composition and photocurrent data allows elucidation of the blending ratios that yield the highest photovoltaic performance. Figure 5e depicts ≈24 000 combinations of composition and photocurrent for the PBDT-TPD:PNDI-T binary, indicating that the optimum blending ratio is close to (70 ± 10) vol% of the donor (PBDT-TPD). Interestingly, optimal performance appears as a smooth (albeit well localized) peak in the composition diagram. Nevertheless, since photocurrent data were generated using monochromatic excitation (488 nm) the optimum D:A ratio found may not correlate perfectly with the optimum encountered under 1 Sun white-light illumination, which for the present blend is close to 1.3:1 (D:A, w:w) or ≈57 wt% of donor.[44] In this regard, the higher absorption of the donor at 488 nm (Figure 4b) supports such a hypothesis. Further photocurrent mapping performed employing the built-in bulb of the Raman acquisition setup indicates as well that the photovoltaic performance peaks close to 70–75 vol% of donor (Figure S12, Supporting Information).

Additionally, note that Raman spectroscopy imaging determines volume fractions, and there may be small differences in density between the donor and acceptor polymers. Regardless, both the reported values and our high-throughput single sample screening consistently indicate that a donor-enriched bulk heterojunction boosts the photovoltaic performance. Conversely, the vertical dispersion observed in the photocurrent (Figure 5e) is attributed to local variations in the total active layer thickness and morphology, which are secondary parameters that require further optimization once the optimum composition has been identified. To this end, we have already demonstrated the rapid and efficient exploration of the active layer thickness dependence through the fabrication of blade-coated thickness gradients,[12] which could complement the herein presented novel optimization approach enabled by microfluidics.

3. Conclusions

In summary, we have introduced a novel processing scheme based on the combination of microfluidics and blade coating to enable the generation of solid-state compositional gradients on surfaces. This methodology is especially appealing for solution-processing organic electronic devices. More particularly, we have demonstrated the fabrication of lateral compositional gradients comprising polymer:fullerene and polymer:polymer blends that are of high current interest in bulk heterojunction OPV devices. The composition profiles achievable using our approach are both smooth and controllable in terms of lateral blending extension, as confirmed by Raman imaging. Indeed, by combining the high-throughput fabrication of lateral compositional gradients with photocurrent mapping of

functional devices, we have successfully shown the optimization of polymer:polymer organic solar cells with optimal use of resources and time.

4. Experimental Section

Materials: PCDTBT, PC$_{70}$BM, and the large-area indium tin oxide (ITO) substrates were purchased from Ossila. P3HT (regio-regular) was purchased from Sigma-Aldrich. N2200 was purchased from Polyera. TQ1 was obtained from 1-Material Organic Nano Electronic. The ZnO nanoparticle dispersion was obtained from Avantama. The polymers PBDT-TPD and PNDI-T were synthesized according to literature protocols.[44]

Sample Preparation: PCDTBT and PC$_{70}$BM were dissolved in chlorobenzene at a concentration of 10 mg mL^{-1}. The ITO substrates were cleaned by consecutive sonication in acetone, a Hellmanex 10% solution in water, isopropanol (5 min each), and sodium hydroxide 10 vol% (10 min), with rinsing in deionized water after each step. The ZnO interlayer was then deposited (50 µL and 40 °C) using an automatic Zehntner ZAA 2300 blade coater with a Zehntner ZUA 2000 aluminum applicator, in air and at a constant speed of 5 mm s^{-1}. The blade gap was set to 200 µm. The active layer was deposited using two NE-1000 pumps manually synchronized with the start of the displacement of the blade coater. A sacrificial substrate (bare glass) was placed prior to the target substrate (ITO + ZnO) until stationary flow conditions were realized at the outlets of the microfluidic array. The bottom transport layer (MoO$_3$) and the Ag electrode were thermally evaporated at a rate of 0.1 and 1 Å s^{-1}, respectively.

Optical Measurements: The optical characterization measurements performed in functional devices, including Raman scattering and light-beam induced current (LBIC), were acquired using a WITec alpha 300 RA+ confocal Raman instrument, coupled to an Olympus objective with 10× magnification (NA 0.25). A solid-state laser operating at 488 nm was employed for both Raman and LBIC measurements. Light was focused through the thick (1.1 mm), ITO-covered glass substrates and the laser power reduced to avoid photodegradation and bleaching of the active layer (3–5 mW at 488 nm in air). Samples were placed on a motorized stage and connected to a DLPCA-200 variable gain low noise current amplifier. All data were collected using WITec Project FIVE software, whilst Raman spectroscopic analysis was performed using a home-made MATLAB routine following a methodology described elsewhere.[43]

Supporting Information

Supporting Information is available from the Wiley Online Library or from the author.

Conflict of Interest

The authors declare no conflict of interest.

Keywords

[1] A. Hein, C. Kortz, E. Oesterschulze, *Sci. Rep.* **2019**, *9*, 15822.

[2] S. Daniel, *Science* **2001**, *291*, 633.

[3] S. L. Vega, M. Y. Kwon, K. H. Song, C. Wang, R. L. Mauck, L. Han, J. A. Burdick, *Nat. Commun.* **2018**, *9*, 614.

[4] S. Fujino, M. Murakami, V. Anbusathaiah, S.-H. Lim, V. Nagarajan, C. J. Fennie, M. Wuttig, L. Salamanca-Riba, I. Takeuchi, *Appl. Phys. Lett.* **2008**, *92*, 202904.

[5] J. C. Meredith, A. Karim, E. J. Amis, *Macromolecules* **2000**, *33*, 5760.

[6] A. Harillo-Baños, X. Rodríguez-Martínez, M. Campoy-Quiles, *Adv. Energy Mater.* **2020**, *10*, 1902417.

[7] M. J. Fasolka, C. M. Stafford, K. L. Beers, in *Polym. Libr.*, (Eds.: M.A.R. Meier, D.C. Webster), Springer, Berlin, Heidelberg **2010**, pp. 63–105.

[8] Y. Imamura, M. Tashiro, M. Katouda, M. Hada, *J. Phys. Chem. C* **2017**, *121*, 28275.

[9] J. Hachmann, R. Olivares-Amaya, A. Jinich, A. L. Appleton, M. A. Blood-Forsythe, L. R. Seress, C. Román-Salgado, K. Trepte, S. Atahan-Evrenk, S. Er, S. Shrestha, R. Mondal, A. Sokolov, Z. Bao, A. Aspuru-Guzik, *Energy Environ. Sci.* **2014**, *7*, 698.

[10] J. Hachmann, R. Olivares-Amaya, S. Atahan-Evrenk, C. Amador-Bedolla, R. S. Sánchez-Carrera, A. Gold-Parker, L. Vogt, A. M. Brockway, A. Aspuru-Guzik, *J. Phys. Chem. Lett.* **2011**, *2*, 2241.

[11] D. Padula, J. D. Simpson, A. Troisi, *Mater. Horiz.* **2019**, *6*, 343.

[12] A. Sánchez-Díaz, X. Rodríguez-Martínez, L. Córcoles-Guija, G. Mora-Martín, M. Campoy-Quiles, *Adv. Electron. Mater.* **2018**, *4*, 1700477.

[13] C. Xie, X. Tang, M. Berlinghof, S. Langner, S. Chen, A. Späth, N. Li, R. H. Fink, T. Unruh, C. J. Brabec, *ACS Appl. Mater. Interfaces* **2018**, *10*, 23225.

[14] S. Chen, Y. Hou, H. Chen, X. Tang, S. Langner, N. Li, T. Stubhan, I. Levchuk, E. Gu, A. Osvet, C. J. Brabec, *Adv. Energy Mater.* **2018**, *8*, 1701543.

[15] C. Yan, S. Barlow, Z. Wang, H. Yan, A. K.-Y. Jen, S. R. Marder, X. Zhan, *Nat. Rev. Mater.* **2018**, *3*, 18003.

[16] A. Facchetti, *Mater. Today* **2013**, *16*, 123.

[17] H. Benten, D. Mori, H. Ohkita, S. Ito, *J. Mater. Chem. A* **2016**, *4*, 5340.

[18] G. Wang, F. S. Melkonyan, A. Facchetti, T. J. Marks, *Angew. Chem., Int. Ed.* **2019**, *58*, 4129.

[19] Y. Meng, J. Wu, X. Guo, W. Su, L. Zhu, J. Fang, Z.-G. Zhang, F. Liu, M. Zhang, T. P. Russell, Y. Li, *Sci. China: Chem.* **2019**, *62*, 845.

[20] Z. Li, X. Xu, W. Zhang, X. Meng, W. Ma, A. Yartsev, O. Inganäs, M. R. Andersson, R. A. J. Janssen, E. Wang, *J. Am. Chem. Soc.* **2016**, *138*, 10935.

[21] J. Nelson, *Mater. Today* **2011**, *14*, 462.

[22] K. Glaser, P. Beu, D. Bahro, C. Sprau, A. Pütz, A. Colsmann, *J. Mater. Chem. A* **2018**, *6*, 9257.

[23] S. Savagatrup, A. D. Printz, T. F. O'Connor, I. Kim, D. J. Lipomi, *Chem. Mater.* **2017**, *29*, 389.

[24] J. Alstrup, M. Jørgensen, A. J. Medford, F. C. Krebs, *ACS Appl. Mater. Interfaces* **2010**, *2*, 2819.

[25] A. Karim, E. Amis, K. Yurekli, R. Krishnamoorti, C. Meredith, *Polym. Eng. Sci.* **2002**, *42*, 1836.

[26] J. B. Thorstenson, L. K. Petersen, B. Narasimhan, *J. Comb. Chem.* **2009**, *11*, 820.

[27] C. M. Stafford, K. E. Roskov, T. H. Epps, M. J. Fasolka, *Rev. Sci. Instrum.* **2006**, *77*, 023908.

[28] R. L. Davis, S. Jayaraman, P. M. Chaikin, R. A. Register, *Langmuir* **2014**, *30*, 5637.

[29] B. Cao, L. A. Adutwum, A. O. Oliynyk, E. J. Luber, B. C. Olsen, A. Mar, J. M. Buriak, *ACS Nano* **2018**, *12*, 7434.

[30] H. Sahu, W. Rao, A. Troisi, H. Ma, *Adv. Energy Mater.* **2018**, *8*, 1801032.

[31] M. Kiy, R. Kern, T. A. Beierlein, C. J. Winnewisser, *Proc. SPIE* **2006**, *6333*, 633307.

[32] S. Langner, F. Häse, J. D. Perea, T. Stubhan, J. Hauch, L. M. Roch, T. Heumueller, A. Aspuru-Guzik, C. J. Brabec, *Adv. Mater.* **2020**, *32*, 1907801.

[33] N. L. Jeon, S. K. W. Dertinger, D. T. Chiu, I. S. Choi, A. D. Stroock, G. M. Whitesides, *Langmuir* **2000**, *16*, 8311.

[34] A. G. G. Toh, Z. P. Wang, C. Yang, N.-T. Nguyen, *Microfluid. Nanofluid.* **2014**, *16*, 1.

[35] S. Cheng, Z. Wu, *Lab Chip* **2012**, *12*, 2782.

[36] C. J. Bettinger, H. A. Becerril, D. H. Kim, B.-L. Lee, S. Lee, Z. Bao, *Adv. Mater.* **2011**, *23*, 1257.

[37] S. Kustra, H. Wu, S. Basu, G. K. Rohde, C. J. Bettinger, *Small* **2012**, *8*, 3746.

[38] P. Carrière, *Phys. Fluids* **2007**, *19*, 118110.

[39] C.-Y. Lee, W.-T. Wang, C.-C. Liu, L.-M. Fu, *Chem. Eng. J.* **2016**, *288*, 146.

[40] C.-Y. Lee, C.-L. Chang, Y.-N. Wang, L.-M. Fu, *Int. J. Mol. Sci.* **2011**, *12*, 3263.

[41] A. I. Shallan, P. Smejkal, M. Corban, R. M. Guijt, M. C. Breadmore, *Anal. Chem.* **2014**, *86*, 3124.

[42] J. M. Cabot, E. Fuguet, M. Rosés, P. Smejkal, M. C. Breadmore, *Anal. Chem.* **2015**, *87*, 6165.

[43] X. Rodríguez-Martínez, M. S. Vezie, X. Shi, I. McCulloch, J. Nelson, A. R. Goñi, M. Campoy-Quiles, *J. Mater. Chem. C* **2017**, *5*, 7270.

[44] X. Xu, Z. Li, W. Zhang, X. Meng, X. Zou, D. Di Carlo Rasi, W. Ma, A. Yartsev, M. R. Andersson, R. A. J. Janssen, E. Wang, *Adv. Energy Mater.* **2018**, *8*, 1700908.